About measuring the stress intensity factor of cracks in curved, brittle shells

Siwen Cao
Department of Mechanics, Materials and Structures, Budapest University of Technology and Economics, Budapest, Hungary
cao.siwen@edu.bme.hu, https://orcid.org/0009-0000-5323-2612

András A. Sipos*
Department of Morphology and Geometric Modeling, Budapest University of Technology and Economics, Budapest , Hungary
HUN-REN-BME Morphodynamics Research Group, Budapest, Hungary
siposa@eik.bme.hu, http://orcid.org/0000-0003-0440-2165

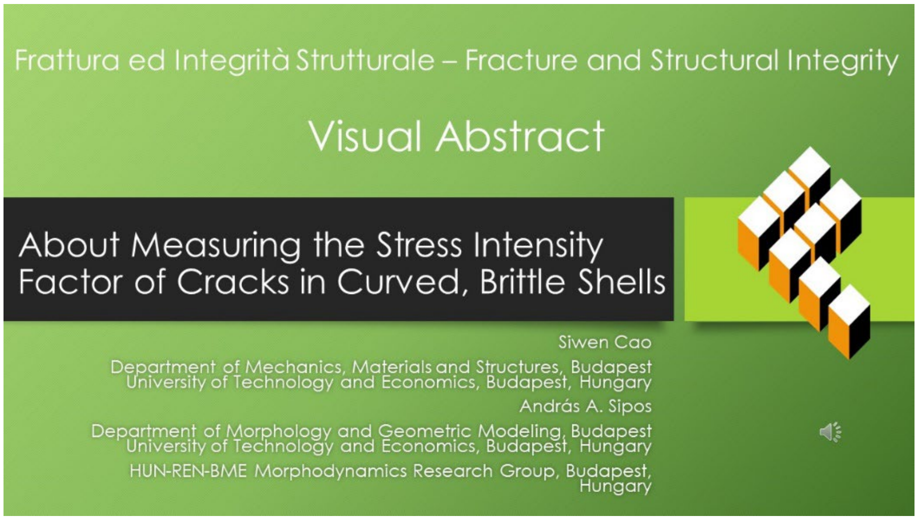

Frattura ed Integrità Strutturale – Fracture and Structural Integrity

Visual Abstract

About Measuring the Stress Intensity Factor of Cracks in Curved, Brittle Shells

Siwen Cao
Department of Mechanics, Materials and Structures, Budapest University of Technology and Economics, Budapest, Hungary
András A. Sipos
Department of Morphology and Geometric Modeling, Budapest University of Technology and Economics, Budapest, Hungary
HUN-REN-BME Morphodynamics Research Group, Budapest, Hungary

Citation: Cao, S., Sipos, A.A., About measuring the stress intensity factor of cracks in curved, brittle shells, Frattura ed Integrità Strutturale, 69 (2024) 1-17.

Received: 19.02.2024
Accepted: 05.04.2024
Published: 13.04.2024
Issue: 07.2024

KEYWORDS. Curved shell, Stress intensity factor, Digital Image Correlation method, Williams expansion, non-developable surface

INTRODUCTION

Fracture of thin curved shells has severe consequences in the broad field of engineering. From pipelines and pressure vessels [1-5], to masonry vaults and concrete shells [6-8], the dominant membrane behavior makes curved shells an efficient structure in countless applications. Since the *membrane behavior* dominantly balances the external actions, the thickness of curved shells tends to be small, meaning that in case of fracture, the entire cross-section becomes cracked instantaneously [9-11]. This situation calls for experimental, analytical, and numerical investigations of crack propagation; however, most of the results of classical fracture mechanics tackle *planar media*.

Specifically, in the realm of linear elasticity, the *Stress Intensity Factor* (SIF) is used to characterize the singular stress distribution

around the crack tip. Keeping the assumption on linear elasticity, the SIF can be relatively easily obtained from displacement measurements on the specimen undergoing fracture. The displacement field in the vicinity of the crack tip can be reliably recorded by Digital Image Correlation (DIC) techniques [12-14], which, due to its simple setting, seems to be gradually eradicating traditional measurement techniques, such as the strain gage method [15] or the photomechanical methods [16-22], regardless a quasi-static or a dynamic problem is studied. Here, we focus on cracks emerging under quasi-static action.
Nonetheless, mechanical assumptions are needed to approximate the SIF from the recorded displacement data. The SIF associated with cracking modes I and II is traditionally derived by the plane stress assumption. Beyond techniques based on the *J-integral* [23-25], the application of the *Willams expansion* [26] is widely adopted. On the one hand, it is consistent with linear fracture mechanics; on the other hand, it operates directly on the displacement field recorded in the vicinity of the crack tip. The truncated Williams series fitted to the displacements delivers the SIF as the first-order coefficient in the expansion. The higher-order terms in the expansion might be associated with non-linearities [27-29], but in an experiment, they also reflect the noise of the testing procedure. Depending on the number of terms in the truncated Williams expansion and the number of data acquisition points, the method leads to an overdetermined system of linear equations, where the best-fit solution is sought. Beyond classical least-square techniques [30,31], there are approaches matched to the finite element method (DIC-FEM)[32] and the extended finite element method (HAX-FEM)[33]. In the case of curved surfaces, the curvature has a non-vanishing effect on the stress distribution, and this contribution is found to be so significant that methods assuming a planar medium fail to recover the SIF faithfully [34,35]. Approaches to developable surfaces exist [36], but a general solution for the problem is still missing.

This paper introduces a new method to obtain the SIF from experimental data of cracks in weakly curved, brittle shells with a non-vanishing Gaussian curvature. In the case of curved shells, the stress in the surfaces depends on the surface's curvature [37]. For shallow shells, this contribution can be easily accounted for; hence, the measured displacements can be readily transformed to *an equivalent planar medium* under plane stress. In the equivalent setting, the application of the Williams expansion is straightforward. As in most engineering applications, the investigated surfaces are weakly curved (i.e., their curvature is moderate), and the cracks are limited in length; we argue the new method is sufficient for most applications to predict the SIF from the measured data reliably.

Specifically, the SIF is obtained via the first-order coefficients of the best-fit Williams expansion. While verifying the method's reliability in experimental work, the tension problem of circumferential cracks in cylindrical shells has been repeated [38], and the obtained test results are compared to theoretical and numerical predictions. Similarly, results on spherical domes are compared against theoretical predictions in the literature. Finally, the convergence properties of the method are studied.

THEORETICAL CONSIDERATIONS

The SIF in Mode 1 and 2 cracking characterizes the stress singularity around the crack tip. This singularity is traditionally studied in a plane stress setting, i.e., for a thin, planar medium with Young modulus E, Poisson ratio ν and thickness h, the T stress tensor and the e infinitesimal strain tensor read:

$$T=\begin{bmatrix} T_{xx} & T_{xy} \\ T_{xy} & T_{yy} \end{bmatrix}=\frac{Eh}{1-\nu^2}\begin{bmatrix} e_{xx}+\nu e_{yy} & (1-\nu)e_{xy} \\ (1-\nu)e_{xy} & \nu e_{xx}+e_{yy} \end{bmatrix} \tag{1}$$

$$e=\begin{bmatrix} e_{xx} & e_{xy} \\ e_{xy} & e_{yy} \end{bmatrix}=\frac{1}{2}\begin{bmatrix} 2\dfrac{\partial u}{\partial x} & \dfrac{\partial u}{\partial y}+\dfrac{\partial v}{\partial x} \\ \dfrac{\partial u}{\partial y}+\dfrac{\partial v}{\partial x} & 2\dfrac{\partial v}{\partial y} \end{bmatrix} \tag{2}$$

where u(x,y) and v(x,y) are the in-plane displacement components. Following the lead of [37] in the case of a shell with moderate curvature, the classical Föppl-von Kármán (FvK) plate equations can be readily extended. Let $W(x,y)$ denote the midsurface of the shell in the reference (unloaded) state, and let the vertical displacement component be $w(x,y)$. In specific, stress T is formally identical to Eqn. (1), but the strain components of the curved shell read:

$$e_{xx} = \frac{\partial u}{\partial x} + \frac{\partial W}{\partial x}\frac{\partial w}{\partial x} + \frac{1}{2}\left(\frac{\partial w}{\partial x}\right)^2 \tag{3}$$

$$e_{xy} = \frac{1}{2}\left(\frac{\partial u}{\partial y} + \frac{\partial v}{\partial x} + \frac{\partial W}{\partial x}\frac{\partial w}{\partial y} + \frac{\partial W}{\partial y}\frac{\partial w}{\partial x} + \frac{\partial w}{\partial x}\frac{\partial w}{\partial y}\right) \tag{4}$$

$$e_{yy} = \frac{\partial v}{\partial y} + \frac{\partial W}{\partial y}\frac{\partial w}{\partial y} + \frac{1}{2}\left(\frac{\partial w}{\partial y}\right)^2 \tag{5}$$

Note that the shear strain e_{xy} defined here is half of the engineering shear strain and $w \equiv 0$ recovers the classical plane stress setting. Similarly, $W \equiv 0$ leads to the FvK plate theory. Nonetheless, measurements can provide the values for u,v,w and W. In our work, we introduce two simplifying assumptions:

i. based on the moderate curvature of the surface, we postulate that the distribution of w around the crack tip is close to linear; i.e., we approximate the non-linear function $w(x,y)$ with its first-order truncated Taylor series. That is

$$w \cong ax + by + c \tag{6}$$

is postulated and the triple (a,b,c) is obtained from the measurements via a least-square fit.

ii. locally, the surface is approximated with a paraboloid.

These two assumptions yield, that we can introduce the displacements $(\bar{u}, \bar{v})$ of the equivalent planar problem, namely:

$$\bar{u} = u + aW(x, y) + \frac{1}{2}a^2 x + \frac{1}{2}aby \tag{7}$$

$$\bar{v} = v + bW(x, y) + \frac{1}{2}b^2 y + \frac{1}{2}abx \tag{8}$$

Substitution of Eqns. (7) and (8) into the expression in Eqn. (2) is identical to the spatial problem in Eqns. (3-5) if assumption (i) is followed. For the sake of completeness, we provide the W_c and W_s formulas for cylindrical and spherical specimens, respectively. In both cases, based on assumption ii. and R denoting the radius of the main circle, we have:

$$W_c(x, y) = -\frac{1}{2R}x^2 \tag{9}$$

$$W_s(x, y) = -\frac{1}{2R}x^2 - \frac{1}{2R}y^2 \tag{10}$$

In summary, the equivalent plane stress problem, characterized by $(\bar{u}, \bar{v})$, provides an identical growth rate of the stress (compared to the curved situation) because the stresses in the shallow shell in the membrane state in the vicinity of the crack tip resembles to a 2D plane stress crack tip, with Eqns. (7) and (8) providing the transformation between the two cases, making the method to a reliable predictor of the SIF.

METHODOLOGY

3D-DIC (digital image correlation) is widely applied in the full-field measurements of deformation and strains in scientific and industrial conditions [39-41], and it can measure the displacement of shell structures like cylindrical structures and spherical structures, as Fig. 1 shows, the components of one 3D-DIC experiment include the specimen, two CCD cameras, and a computer. For improved visibility, the relevant region of the specimen surface is painted with artificial speckles; during the loading process, two CCD cameras capture images simultaneously. After the experiment, the displacement field with components stored in vectors **U**, **V**, and **W** in a global frame at each time instant can be retrieved.

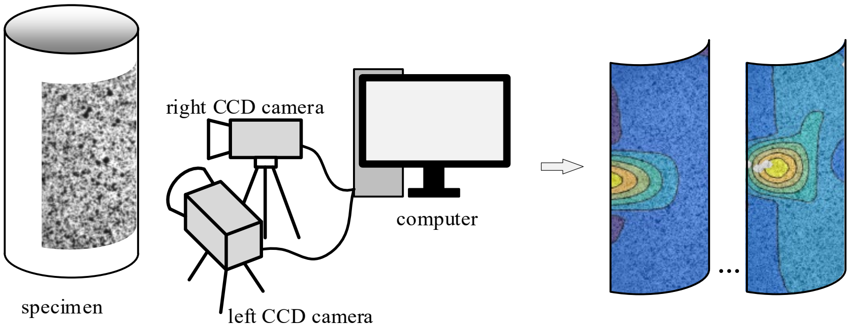

Figure 1: Components of 3D-DIC and results of displacement field.

To calculate the stress intensity factor of a curved shell, as Fig. 2 (a) shows, the tangent to the surface is located at the crack tip. Denote the unit normal vector of the surface at the crack tip to $\boldsymbol{k}$, the unit vector in the tangent plane directed along the extended crack to $\boldsymbol{i}$, and set $\boldsymbol{j} = \boldsymbol{k} \times \boldsymbol{i}$, where '×' denotes the cross product. The displacement component vectors **U**, **V**, **W** in the global basis ($\boldsymbol{x}$, $\boldsymbol{y}$, $\boldsymbol{z}$) can be transformed to the local basis ($\boldsymbol{i}$, $\boldsymbol{j}$, $\boldsymbol{k}$) via:

$$\begin{bmatrix} \mathbf{u} \\ \mathbf{v} \\ \mathbf{w} \end{bmatrix} = \mathbf{A}_{(x,y,z)\rightarrow(i,j,k)} \begin{bmatrix} \mathbf{U} \\ \mathbf{V} \\ \mathbf{W} \end{bmatrix} \tag{11}$$

where matrix $\mathrm{A}_{(x,y,z)\rightarrow(i,j,k)}$ is the transformation matrix from basis ($\boldsymbol{x}$, $\boldsymbol{y}$, $\boldsymbol{z}$) to the basis ($\boldsymbol{i}$, $\boldsymbol{j}$, $\boldsymbol{k}$), and **u**, **v**, **w** are the displacement component vectors in basis ($\boldsymbol{i}$, $\boldsymbol{j}$, $\boldsymbol{k}$). The displacement component **w** is normal to the tangent plane spanned by $\boldsymbol{i}$ and $\boldsymbol{j}$, which means the 2D displacement components are vectors **u**, **v**.

In the following step, the elements of **w** is used to fit a plane and obtain the constants (a,b,c), as it is described in the previous section. In order to compute $(\bar{\mathrm{u}}, \bar{\mathrm{v}})$ in Eqns. (7) and (8), we need W. It is either measured in the unloaded state, or in the case of simple geometries, it is known a-priori, as it is given for a cylinder (with a horizontal crack) in Eqn. (9) or for the sphere in Eqn. (10). The values of the equivalent displacements $(\bar{\mathrm{u}}, \bar{\mathrm{v}})$ are stored in the vectors $\bar{\mathrm{u}}$ and $\bar{\mathrm{v}}$.

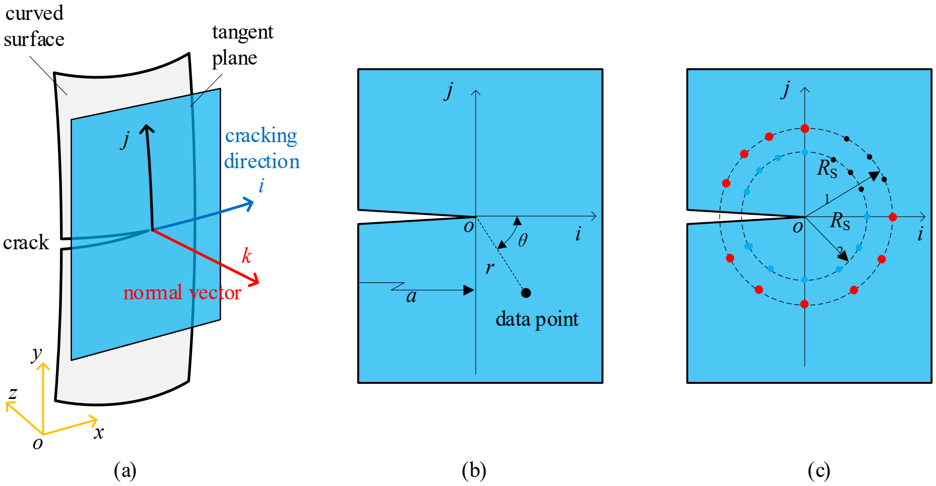

(a) (b) (c)

Figure 2: Projection of the displacements and selection of data points on the tangent plane. (a) placement of the tangent plane and the local basis ($\boldsymbol{i}$, $\boldsymbol{j}$, $\boldsymbol{k}$). (b) the local basis and the applied polar coordinates at the crack tip. (c) Data selection ring with the radius R_s.

Then, with the equivalent 2D displacement component vectors $\bar{\mathrm{u}}$ and $\bar{\mathrm{v}}$, the computation of the stress intensity factor can be carried out via the Williams expansion [23]. As Fig. 2 (b) shows, the $\boldsymbol{i}$-axis of the local basis is aligned with the extending direction, i.e., the tangent vector of the crack's curve. The polar coordinates with angle θ and radius r are introduced. On the data selection ring around the crack tip, the displacement components $\overline{\mathrm{u}}$ and $\overline{\mathrm{v}}$ are determined from the displacement component vectors $\overline{\mathrm{u}}$ and $\overline{\mathrm{v}}$ by interpolation. Note that the number of data points D_{N} and the ring radius R_{S} are free parameters in the method and affect the convergence rate (see later). Then, the in-plane displacement field around any crack can be expressed with the help of the following Williams expansion:

$$\begin{aligned}\begin{Bmatrix}\overline{u}\\ \overline{v}\end{Bmatrix} &= \sum_{n=0}^{\infty}\frac{A_n}{2G}r^{n/2}\begin{Bmatrix}\left(\kappa+\frac{n}{2}+(-1)^n\right)\cos\frac{n}{2}\theta-\frac{n}{2}\cos(\frac{n}{2}-2)\theta\\ \left(\kappa-\frac{n}{2}-(-1)^n\right)\sin\frac{n}{2}\theta+\frac{n}{2}\sin(\frac{n}{2}-2)\theta\end{Bmatrix}\\ &+\sum_{n=0}^{\infty}\frac{B_n}{2G}r^{n/2}\begin{Bmatrix}\left(-\kappa-\frac{n}{2}+(-1)^n\right)\sin\frac{n}{2}\theta+\frac{n}{2}\sin(\frac{n}{2}-2)\theta\\ \left(\kappa-\frac{n}{2}+(-1)^n\right)\cos\frac{n}{2}\theta+\frac{n}{2}\cos(\frac{n}{2}-2)\theta\end{Bmatrix}\end{aligned} \tag{12}$$

where G is the material's shear modulus, $\overline{\mathrm{u}}$ and $\overline{\mathrm{v}}$ are the ***i*** and ***j***-directed displacement components. $\kappa=(3-\nu)/(1+\nu)$ for plane stress. A_{n} and B_{n} are the coefficients of the Williams expansion. In specific, four coefficients among A_{n} and B_{n} are essential for fracture mechanics [42]:

$$\begin{aligned}&A_0=\frac{u_0 2G}{\kappa+1}\\ &A_1=\frac{K_{\mathrm{I}}}{\sqrt{2\pi}}\\ &B_0=\frac{v_0 2G}{\kappa+1}\\ &B_1=-\frac{K_{\mathrm{II}}}{\sqrt{2\pi}}\\ &B_2=-\varphi_c 2G/\left(\kappa+1\right)\end{aligned} \tag{13}$$

Here u_0 and v_0 are the rigid body displacement, φ_{c} is the rigid body rotation to the crack tip, and K_{I} and K_{II} are the stress intensity factors for mode I and mode II cracks, respectively. For details, we refer to [42-44]. In this paper, we study a problem where a mode I crack is dominant [38]; hence, we aim to approximate A_1, and consequently, K_{I} can be computed by Eqn. (13).

The T_{N} number of terms in the truncated Williams expansion should be sufficiently large to calculate the SIF with high precision. Nonetheless, the D_{N} number of data points should be equal to or exceed (T_{N}+1) [42,23]:

$$D_{\mathrm{N}} \geq T_{\mathrm{N}}+1 \tag{14}$$

Following Fig. 2 (c), the local coordinate basis (in particular, the location of the crack tip and the crack orientation) is detected and corrected by the user manually (since the notches are pre-cut, these parameters are easily determined.). The data points are selected on data-selecting rings surrounding the crack tip with different radii R_{S1}, R_{S2}, …etc. These radii should be sufficiently big to avoid the intensively nonlinear zone around the crack tip [45]. The size of the region varied from specimen to specimen and can be determined from the strain-field contour obtained by the DIC method.

For any data point i, the coordinates θ_i, and r_i are given by the location of the point, and its displacements u_{i} and v_{i} are obtained from the DIC data. The truncated Williams expansion up to the term T_{N} readily follows in a matrix form:

$$\begin{bmatrix} \overline{u}_1 \\ \overline{u}_2 \\ \vdots \\ \overline{u}_{D_\mathrm{N}} \\ \overline{v}_1 \\ \overline{v}_2 \\ \vdots \\ \overline{v}_{D_\mathrm{N}} \end{bmatrix} = \begin{bmatrix} f_{\mathrm{A}_0}(r_1,\theta_1) & f_{\mathrm{B}_0}(r_1,\theta_1) & f_{\mathrm{A}_1}(r_1,\theta_1) & f_{\mathrm{B}_1}(r_1,\theta_1) & \cdots & f_{\mathrm{A}_{T_\mathrm{N}}}(r_1,\theta_1) & f_{\mathrm{B}_{T_\mathrm{N}}}(r_1,\theta_1) \\ f_{\mathrm{A}_0}(r_2,\theta_2) & f_{\mathrm{B}_0}(r_2,\theta_2) & f_{\mathrm{A}_1}(r_2,\theta_2) & f_{\mathrm{B}_1}(r_2,\theta_2) & \cdots & f_{\mathrm{A}_{T_\mathrm{N}}}(r_2,\theta_2) & f_{\mathrm{B}_{T_\mathrm{N}}}(r_2,\theta_2) \\ \vdots & \vdots & \vdots & \vdots & \ddots & \vdots & \vdots \\ f_{\mathrm{A}_0}(r_{D_\mathrm{N}},\theta_{D_\mathrm{N}}) & f_{\mathrm{B}_0}(r_{D_\mathrm{N}},\theta_{D_\mathrm{N}}) & f_{\mathrm{A}_1}(r_{D_\mathrm{N}},\theta_{D_\mathrm{N}}) & f_{\mathrm{B}_1}(r_{D_\mathrm{N}},\theta_{D_\mathrm{N}}) & \cdots & f_{\mathrm{A}_{T_\mathrm{N}}}(r_{D_\mathrm{N}},\theta_{D_\mathrm{N}}) & f_{\mathrm{B}_{T_\mathrm{N}}}(r_{D_\mathrm{N}},\theta_{D_\mathrm{N}}) \\ g_{\mathrm{A}_0}(r_1,\theta_1) & g_{\mathrm{B}_0}(r_1,\theta_1) & g_{\mathrm{A}_1}(r_1,\theta_1) & g_{\mathrm{B}_1}(r_1,\theta_1) & \cdots & g_{\mathrm{A}_{T_\mathrm{N}}}(r_1,\theta_1) & g_{\mathrm{B}_{T_\mathrm{N}}}(r_1,\theta_1) \\ g_{\mathrm{A}_0}(r_2,\theta_2) & g_{\mathrm{B}_0}(r_2,\theta_2) & g_{\mathrm{A}_1}(r_2,\theta_2) & g_{\mathrm{B}_1}(r_2,\theta_2) & \cdots & g_{\mathrm{A}_{T_\mathrm{N}}}(r_2,\theta_2) & g_{\mathrm{B}_{T_\mathrm{N}}}(r_2,\theta_2) \\ \vdots & \vdots & \vdots & \vdots & \ddots & \vdots & \vdots \\ g_{\mathrm{A}_0}(r_{D_\mathrm{N}},\theta_{D_\mathrm{N}}) & g_{\mathrm{B}_0}(r_{D_\mathrm{N}},\theta_{D_\mathrm{N}}) & g_{\mathrm{A}_1}(r_{D_\mathrm{N}},\theta_{D_\mathrm{N}}) & g_{\mathrm{B}_1}(r_{D_\mathrm{N}},\theta_{D_\mathrm{N}}) & \cdots & g_{\mathrm{A}_{T_\mathrm{N}}}(r_{D_\mathrm{N}},\theta_{D_\mathrm{N}}) & f_{\mathrm{B}_{T_\mathrm{N}}}(r_{D_\mathrm{N}},\theta_{D_\mathrm{N}}) \end{bmatrix} \begin{bmatrix} \mathrm{A}_0 \\ \mathrm{B}_0 \\ \mathrm{A}_1 \\ \mathrm{B}_1 \\ \vdots \\ \mathrm{A}_{T_\mathrm{N}} \\ \mathrm{B}_{T_\mathrm{N}} \end{bmatrix} \quad (15)$$

where the functions in the coefficient matrix are given by

$$\begin{aligned} f_{\mathrm{A}_n}(r,\theta) &= \frac{r^{n/2}}{2G}\left[\left(\kappa+\frac{n}{2}+(-1)^n\right)\cos\frac{n}{2}\theta-\frac{n}{2}\cos(\frac{n}{2}-2)\theta\right], \\ f_{B_n}(r,\theta) &= \frac{r^{n/2}}{2G}\left[\left(-\kappa-\frac{n}{2}+(-1)^n\right)\sin\frac{n}{2}\theta+\frac{n}{2}\sin(\frac{n}{2}-2)\theta\right], \\ g_{A_n}(r,\theta) &= \frac{r^{n/2}}{2G}\left[\left(\kappa-\frac{n}{2}-(-1)^n\right)\sin\frac{n}{2}\theta+\frac{n}{2}\sin(\frac{n}{2}-2)\theta\right], \\ g_{B_n}(r,\theta) &= \frac{r^{n/2}}{2G}\left[\left(\kappa-\frac{n}{2}+(-1)^n\right)\cos\frac{n}{2}\theta+\frac{n}{2}\cos(\frac{n}{2}-2)\theta\right]. \end{aligned} \quad (16)$$

Eqn. (16) can be written as:

$$\mathbf{U}_{2D_\mathrm{N},1} = \mathbf{C}_{2D_\mathrm{N},2T_\mathrm{N}+2}\mathbf{A}_{2T_\mathrm{N}+2,1} \quad (17)$$

where vector **A** contains the unknown coefficients of the Williams expansion. If $2D_\mathrm{N}>2T_\mathrm{N}+2$, then matrix **C** is rectangular, and the system is overdetermined. Utilizing the generalized inverse of **C**, vector **A** can be obtained via

$$\boldsymbol{A} = (\boldsymbol{C}^T\boldsymbol{C})^{-1}\boldsymbol{C}^T\boldsymbol{U} \quad (18)$$

In fact, Eqn. (18) yields the solution of Eqn. (17) with the minimal least-squares error.

CYLINDRICAL SHELLS

Cylinder shell structures are used in this chapter to execute and validate the method for the detection of SIF on curved surface shells. For the experiments, the tensile test of polymethyl methacrylate (PMMA) cylindrical shell specimens (shown in Fig. 3(a)) was carried out; the mechanical properties and dimensions are shown in Tab. 1. Through cracks of specimens were cut by 0.25 mm diameter diamond wire saws, and the length of the crack is denoted by its central angle $2a$ ($2a$=30°, 60°, 90°, 120°, 150°, and 180°, respectively). Fig. 3 (b) shows that the specimen is under displacement-controlled tension; the loading rate is kept at 0.25 mm/min using a Zwick/Roell Z-150 testing machine to prevent the interference of dynamic actions (i.e., a quasi-static load). Fig. 3 (c) shows the clamped support of the cylinder specimens. The upper and lower parts of the specimen are fixed by specially designed fixtures, which are fastened with two sets of hose clamps. Sand the ends of the specimen with sandpaper for firmer clamps. The length of the clamps are 15mm. The 3D deformation data on the surface of specimens are obtained by a 3D-DIC system produced by Correlated Solutions, Inc., the capture frequency of photos was 1 Hz. To reduce the environmental effect, the DIC-3D system calculated the average of 5 sets of photos at a time. The vertical distance between two cameras and the specimen is 0.6 m, and the angle between the two cameras is 6.68°. The subset size was 11×11 pixels, the diameters of the speckles varied between 0.01~0.05mm. The test stopped when the specimen broke. Each test was repeated three times.

Modulus of elasticity E [MPa]	Poisson's ratio ν	Length L [mm]	Thickness h [mm]	Radius R [mm]
3300	0.37	120.0	2.0	20.0

Table 1: The material parameters and geometric properties of the cylinder model

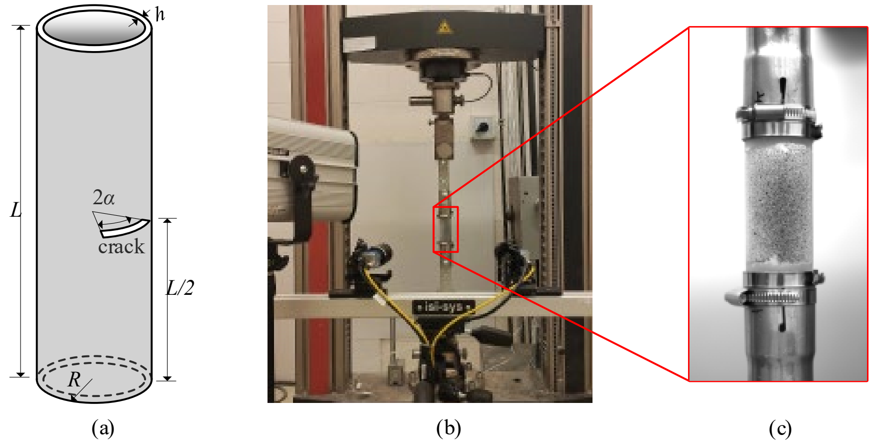

Figure 3: Experimental setup. (a) shape and dimensions of the cylindrical shell structure (b) the loading and observing of the cylinder specimen. (c) the way of specimens clamping.

Meanwhile, the numerical displacement field was simulated by Abaqus 2017 with a linear elastic constitutive equation. The dimensions and mechanical properties of the numerical models were identical to the experimental specimens; the setting of boundary conditions is shown in Fig. 4 (a), and all DoFs at the bottom of the cylinder are fixed. At the top, all DoFs, except the axial direction, are also fixed. The loading force varies from 0 N to 3000 N along the axial direction during 300 s. The finite element mesh type in Fig. 4 (d) is hexahedral (C3D8R), and the characteristic length of the mesh reads 1 mm.

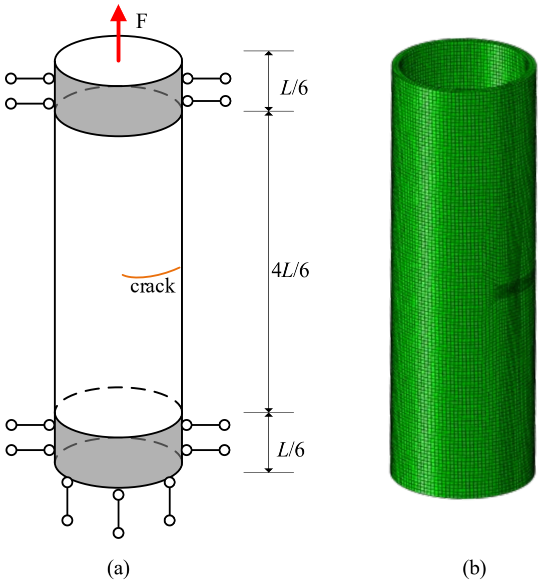

Figure 4: Cylindrical shell numerical simulation (a) FEM cylinder model for numerical validation. (b) The FEM mesh model used in the numerical simulation.

Fig. 5 (a) shows the curves of both K_I and K_{II} for increasing tensile stress from experimental specimens EA30, EA30-1, and EA30-2 and the numerical specimen NA30. Nonetheless, the curve of the numerical model is a straight line for both K_I and K_{II}, but they exhibit fluctuations in the experiments. This happens because the deformation data from the numerical simulation is smooth. On the contrary, the experimental deformation data are affected by noise. Still, the SIF curves of experimental specimens agree with the trend of the numerical results. Due to the uniaxial tension, we expect a mode I crack. Our results agree with this expectation: the mode I stress intensity factor K_I shows an upward trend, while the mode II stress intensity factor K_{II} remains around zero.

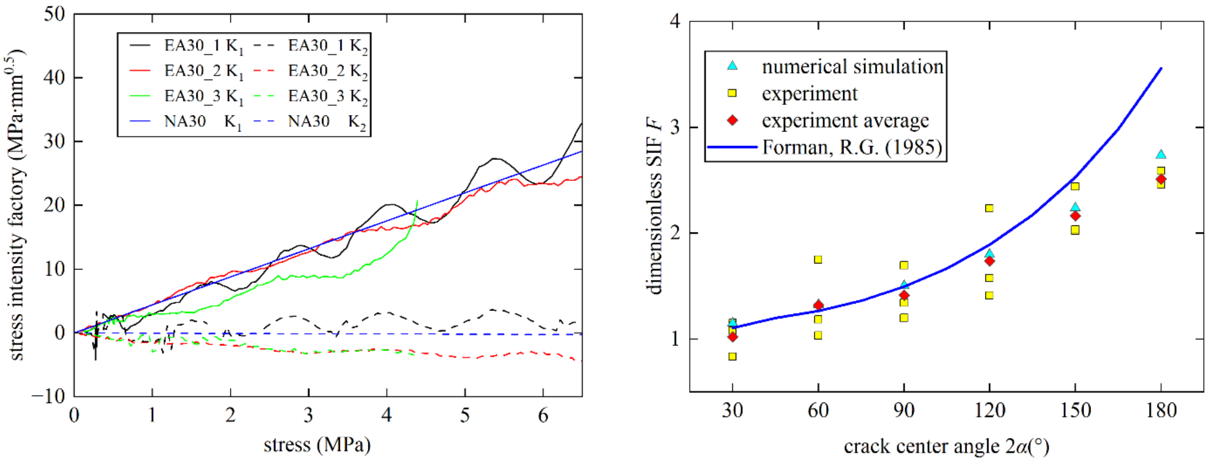

(a) (b)

Figure 5: Stress intensity factor results of cylindrical shell. (a)SIF (K_I, K_{II})-stress curves at increasing tensile stress for specimens/model with center angle 2α=30°. (b) Dimensionless SIF comparison of theory, experimental, and numerical simulation results for the cylindrical shell.

The experimental, numerical, and theoretical predictions were compared via the dimensionless SIF *F*, defined as follows:

$$F = K_I / \sigma\sqrt{\pi a} \tag{19}$$

Tab. 2 shows the results of all experimental specimens and numerical models, and Fig. 5 (b) depicts the dimensionless SIF comparison of theoretical, experimental, and numerical simulation results. From the table, the difference between experimental specimens, numerical models, and theoretical value with small center angle cracks is evidentially smaller than for the large center angle cracks, which trend is more apparent in Fig. 5 (b). The dimensionless SIF *F* curve of Forman, R. G. [38] changing by crack center angle 2*a* in Fig. 5 (b) shows an upward trend. The experimental and numerical results are scattered around this theoretical solution. The average result of the repeated experiments (with the same crack center angle) is also added to Fig. 5 (b) to highlight the overall trend of all experimental and numerical outcomes. When the crack central angle is between 30° and 120°, the mean results of the experimental and numerical results are close to the theoretical curve. At 2α=150° and 2α =180°, all testing results are smaller than the theoretical value, which can be reflected by results from numerical simulation.

Crack center angle 2*a*	30°	60°	90°	120°	150°	180°
Experimental	1.15	1.18	1.34	2.23	2.02	2.48
	1.08	1.03	1.70	1.57	2.44	2.59
	0.83	1.75	1.20	1.41	2.03	2.46
numerical	1.15	1.32	1.50	1.80	2.24	2.73
Forman, R. G.	1.10	1.27	1.50	1.89	2.53	3.56

Table 2: Dimensionless SIF results of cylindrical experimental specimens, numerical models, and Forman, R. G.'s research [38].

SPHERICAL SHELLS

Spherical shell structures are used in this chapter to verify the suitability of the displacement method for non-developable surfaces. Erdogan, F. [46] research the SIF for the crack on a sphere loaded by a uniform membrane load. To compare the results of Erdogan's research, numerical simulations are conducted by ABAQUS 2017 with a linear elastic constitutive equation. The numerical simulation model dimensions and mechanical properties are shown in Tab. 3, which refers to the properties of spherical shell experimental specimens and the research of Erdogan, F., and the max crack length of Erdogan, F.'s research is 78.97°, the crack length $2a$ of models is set as 16°, 32°, 48°, 64°, 80°. The setting of boundary conditions is shown in Fig. 6(a); at the bottom of the spherical model, the DoF of the vertical direction is fixed, and the total membrane force perpendicular to the crack varies from 0 N to 300 N during 300 s. The finite element mesh type in Fig. 6 (b) is hexahedral (C3D8R), and the characteristic length of the mesh reads 1.25 mm.

Modulus of elasticity E [MPa]	Poisson's ratio ν	Thickness h [mm]	Radius R [mm]
3300	0.33	5.0	100.0

Table 3: The material parameters and geometric properties of the spherical model.

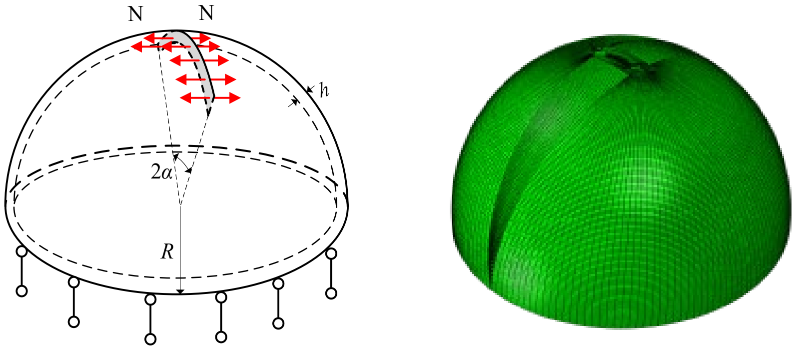

(a)

(b)

Figure 6: spherical shell numerical simulation (a) FEM spherical model for numerical validation. (b) The FEM mesh model used in the numerical simulation.

Crack center angle $2a$	16°	32°	48°	64°	80°
numerical	1.90	1.90	2.65	3.64	4.63
Erdogan, F.	1.26	1.80	2.45	3.19	4.00

Table 4: Dimensionless SIF results of numerical spherical models, and the Erdogan, F.'s research

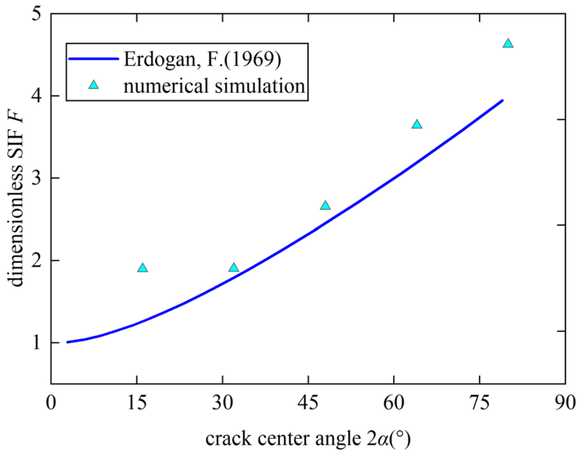

Figure 7: Dimensionless SIF comparison of theory and numerical simulation results for a spherical shell.

The results of dimensionless SIF detected by the new method are summarized in Tab. 4 and Fig. 7; the dimensionless SIF F of Erdogan, F. in the table is calculated by linear interpolation. According to Fig. 7 the method can be used for non-developable surfaces; the result of dimensionless SIFs meets the result of Erdogan, F.'s well between 30° to 60°, and the values are all larger than Erdogan, F. for other crack lengths.

CONVERGENCE FEATURES

Based on the Methodology section, the F dimensionless SIF is affected by T_N number of terms in the truncated Williams expansion, the D_N number of data points, and the R_s data selection radius. To investigate the influence of those factors on the convergence of F clearly, the experimental data of cylindrical shell structure specimens/models are used below. The E_N exceed number of D_N to T_N is defined as:

$$E_N = D_N - T_N - 1 \tag{20}$$

Meanwhile, to separate each specimen clearly, all labels of specimens shown in Tab. 5.

Crack center angle 2α	30º	60º	90º	120º	150º	180º
Experimental specimen	EA30_1	EA60_1	EA90_1	EA120_1	EA150_1	EA180_1
	EA30_2	EA60_2	EA90_2	EA120_2	EA150_2	EA180_2
	EA30_3	EA60_3	EA90_3	EA120_3	EA150_3	EA180_3
Numerical model	NA30	NA60	NA90	NA120	NA150	NA180

Table 5: Label of cylindrical shell structure specimens/models.

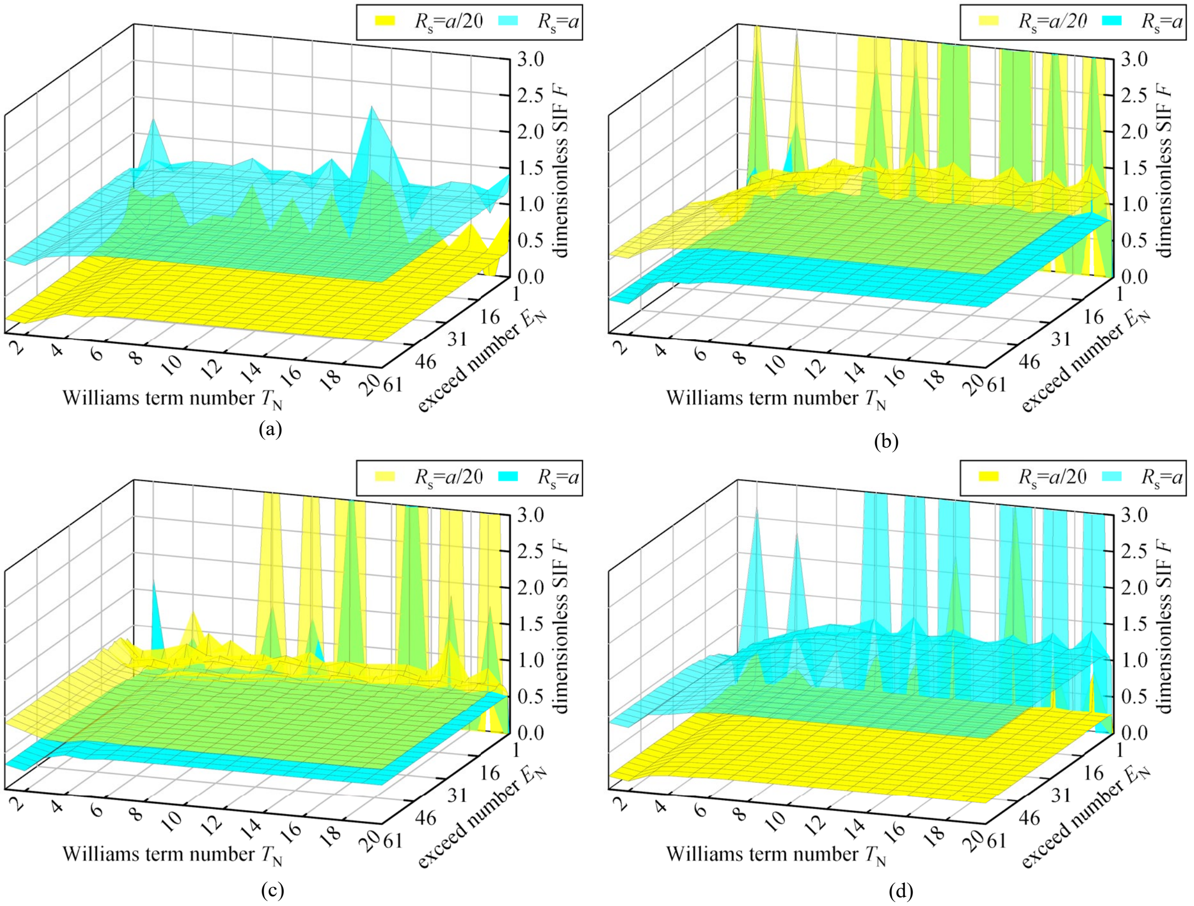

(a)

(b)

(c)

(d)

Figure 8: dimensionless SIF F surfaces with different R_S, T_N, and E_N for specimens/model with crack center angle $2a$=30°. (a) dimensionless SIF F surfaces of NA30 (b) dimensionless SIF F surfaces of EA30_1. (b) dimensionless SIF F surfaces of EA30_2. (d) dimensionless SIF F surfaces of EA30_3.

Fig. 8 shows the F dimensionless SIF surfaces with different R_S, T_N, and E_N for specimens/model at a crack center angle of 30°, (a) is the F surface of NA30, and (b)-(d) is the F surface for samples EA30-1, EA30-2, and EA30-3, respectively. It is evident that with increasing T_N and E_N, the F result is convergent to a steady value. It is also clear that D_N should not only satisfy Eqn. (14), when E_N =1. From Fig. 8, the result of F fluctuates wildly with the changes of T_N, and when E_N becomes somewhat bigger, then fluctuations disappear. Meanwhile, from Fig. 8 (d), for EA30-3, when T_N is less than 6, the steady value of F differs and increases; this phenomenon can also be observed in other panels of Fig. 8, and when T_N is large enough, then the steady value of F is close for all specimens/model.

The results of F with different data selecting ring radius R_S exhibit more evident discrepancies than the cases of varying E_N or T_N. A change in R_S can shift the final steady F significantly, especially for NA30 (Fig. 8 (a)) and EA30-3(Fig. 8 (d)), and the difference for F with different R_S of EA30-1 is the smallest.

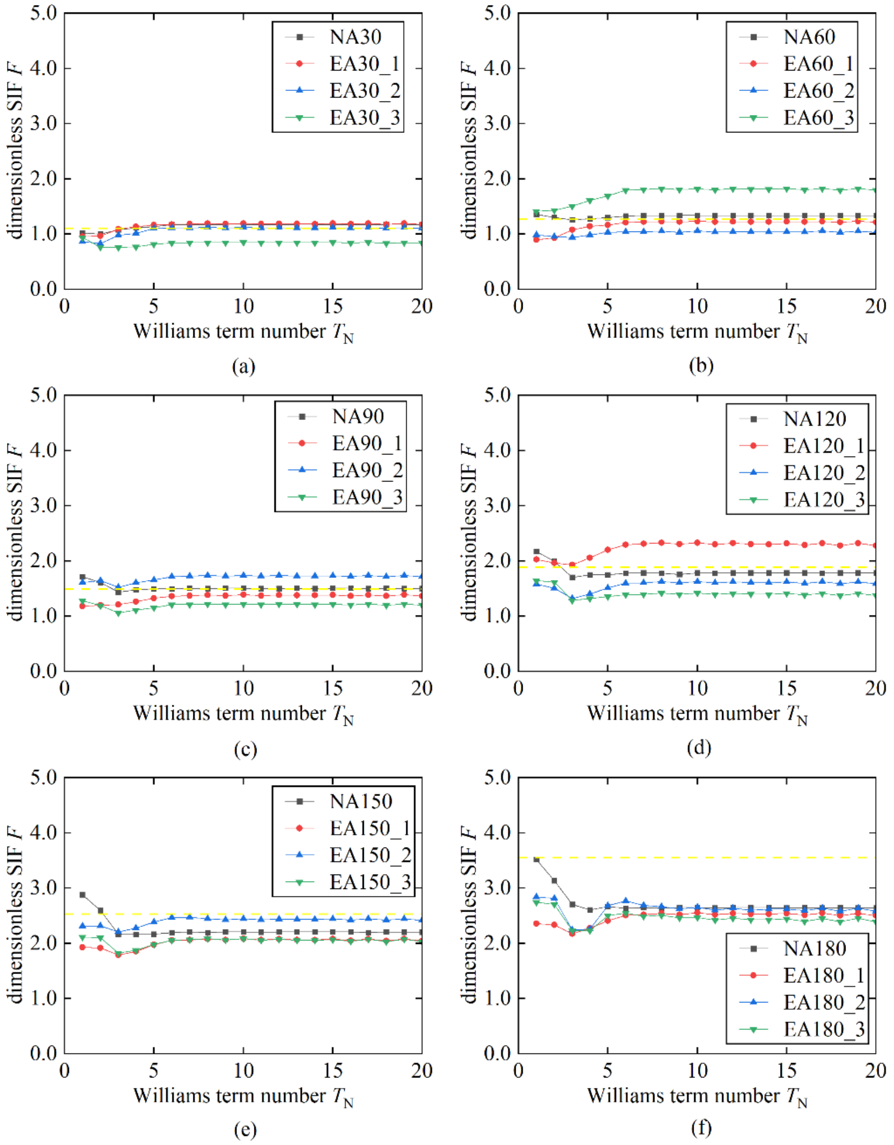

Figure 9: F- T_N curves for all experimental specimens and numerical models. (a) $2a=30^{\circ}$. (b) $2a=60^{\circ}$. (c) $2a=90^{\circ}$. (d) $2a=120^{\circ}$. (e) $2a=150^{\circ}$. (f) $2a=180^{\circ}$.

Since the singular stress term dominates the crack-tip stress field, the higher-order terms are usually neglected in previous studies of brittle materials [47-50]. However, sometimes, the higher-order terms in the Williams expansion cannot be thoughtlessly ignored [51]. Fig. 9 shows F- T_N curves for all experimental specimens and numerical models; the yellow dash in the figures is the theoretical value. When T_N is less than 6, F for all specimens/models varies, and when T_N is larger than 6, F converges gradually. Meanwhile, the steady value of F for specimens/models whose crack center angle is in the range of 30°-90° has good agreement with the corresponding theoretical value. For specimens/models whose crack center angle is 120° and 150°, the results from the numerical model and one of the experimental specimens agree well with the corresponding theoretical value. For specimens/models with a 180° center angle crack, both the numerical model's steady result and all experimental results differ from the theoretical value.

The F- E_N curves for all experimental samples and numerical models are given in Fig. 10. Unlike the influence of T_N on the convergence, as shown in Fig. 8 above, when E_N is somewhat bigger than 1, the results of F can exhibit a convincing convergence. Still, the discrepancies at high center angle cracks prevail.

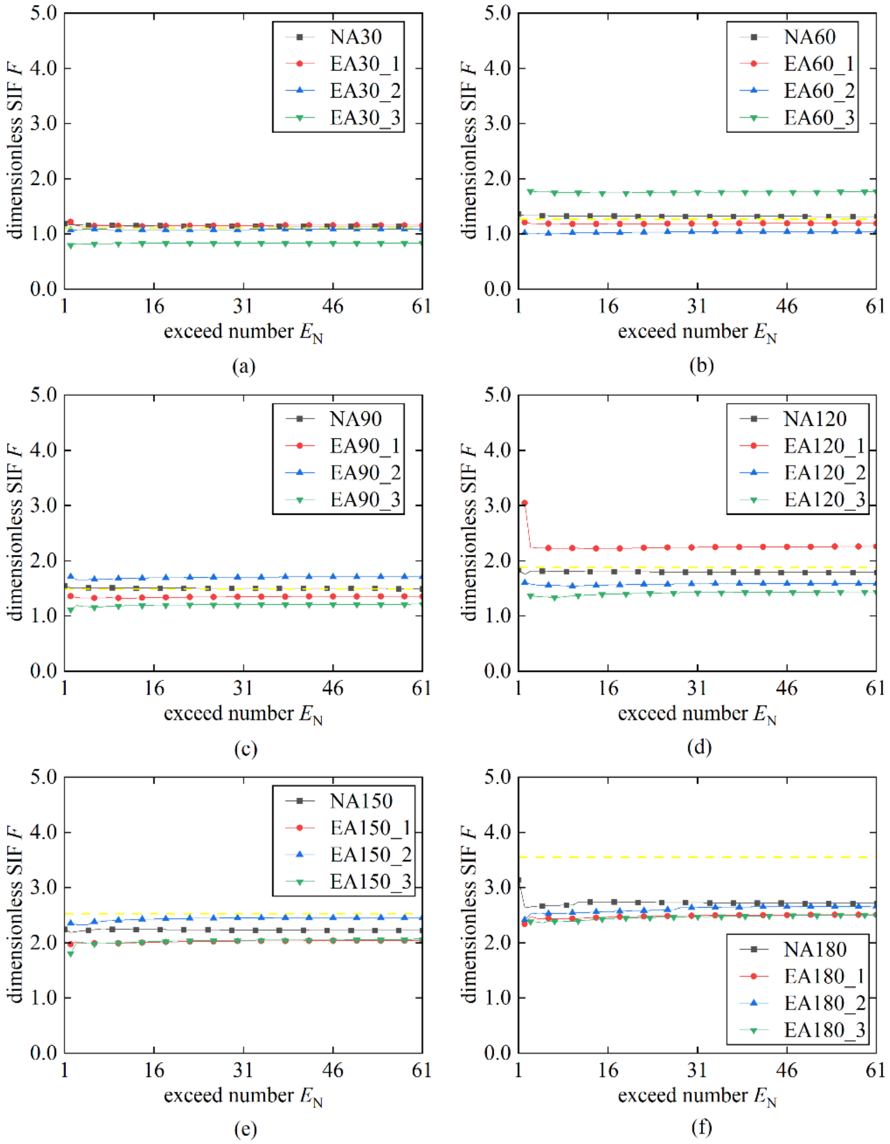

Figure 10: F- E_N curves for all experimental specimens and numerical models. (a) $2a$=30°. (b) $2a$=60°. (c) $2a$=90°. (d) $2a$=120°. (e) $2a$=150°. (f) $2a$=180°.

We found that the differences between the experimental and the numerical data and the influence of crack length on the F dimensionless SIF with comparable data selecting ring radius R_S for specimens/model is apparent; we investigated the case when data selecting ring radius R_s depends on the crack length a.

Fig. 11 shows that for all numerical models whose crack center angle is between 30° and 120°, the F results converge to the theoretical value's neighborhood. For numerical models whose crack center angle is 150° and 180°, the best value of R_s/a is between 0.4 and 0.5. Moreover, for all experimental specimens in the crack center angle range of 30° to 150°, with increasing R_s/a, the value of F converges gradually, and the appropriate value of R_s/a exceeds 0.3. Experimental specimens with a 180° crack center angle still do not converge, corresponding to the limitations of 3D DIC recording of the 3D deformation fields.

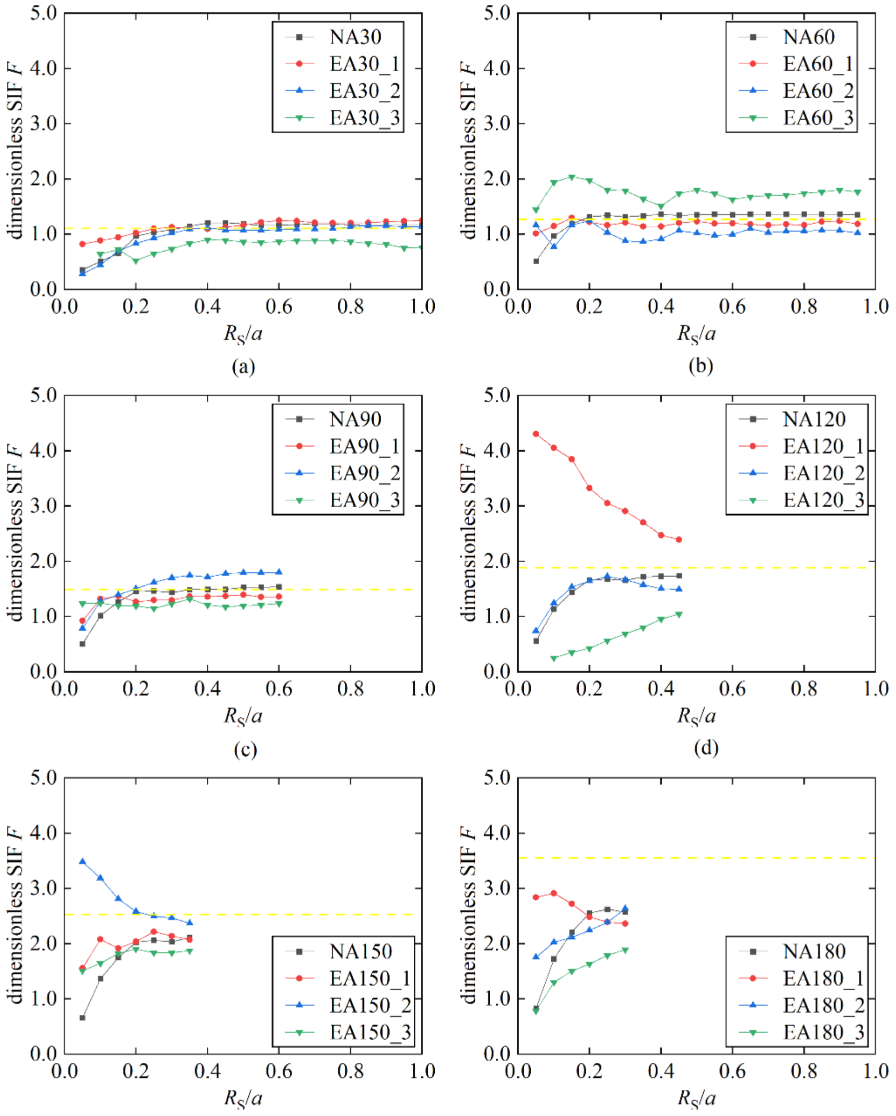

(a) (b) (c) (d) (e) (f)

Figure 11: F-(R_S/a) curves for all experimental specimens and numerical models. (a) $2a=30°$. (b) $2a=60°$. (c) $2a=90°$. (d) $2a=120°$. (e) $2a=150°$. (f) $2a=180°$.

DISCUSSION

Since the deformation field calculated by the DIC method is on the surface of the specimen, and the fracture energy is stored at the entire fracture surface, the calculation results of this method will have larger errors for thicker specimens. In fact, for thick-walled cylindrical shells, the stress states are different in the middle and on the sides: the middle is in the plane strain condition, and the two sides are close to the plane stress condition. Therefore, during the loading process, the shape of the plastic zone at the crack tip changes with the thickness. Based on the Mises yield criterion [52], the radius of the plastic zone should read

$$r_{pl}=\frac{1}{2\pi}\left(\frac{K_{\rm I}}{\sigma}\right)^2\left[\frac{1}{2}\left(1+\cos\theta\right)+\frac{3}{4}\sin^2\theta\right],\quad \text{(plane stress)} \tag{21}$$

$$r_{pl} = \frac{1}{2\pi}\left(\frac{K_{\mathrm{I}}}{\sigma}\right)^2 \left[\left(1-2\upsilon\right)^2\left(1+\cos\theta\right)+\frac{3}{4}\sin^2\theta\right]. \quad \text{(plane strain)} \qquad (22)$$

Eqns. (21) and (22) show that the area of the plastic zone in the plane strain condition (triaxial stress state) is significantly smaller than in the plane stress condition. It follows, that the method should be applied for sufficiently thin shells, as solely the displacements of the outer surface is recorded.

CONCLUSIONS

This paper proposes a method to calculate the SIF from experimental data for developable and non-developable surfaces with small or moderate curvature. The new method, is based on the truncated Williams expansion of the equivalent displacement field, obtained by assuming a shallow shell and taking its curvature into account. To verify the method, the tension problem of circumferential cracks in cylindrical shells is studied. The experimental results are compared against theoretical and numerical predictions on the same problem. Then, the method is applied to the calculation of crack tip SIF on a hemispherical dome and compared with the theoretical solution. The following conclusions can be drawn:

(1) The repeated experimental and numerical simulation results are close.
(2) The method can be used for non-developable surfaces with a moderate Gaussian curvature. For a hemispherical shell, the result of dimensionless SIFs meets the results by Erdogan, F.'s for crack angles well between 30º to 60º.
(3) The T_{N} number of terms in the Williams expansion affects the method's accuracy. Convergence in the SIF requires T_{N} to exceed 6.
(4) For different geometries, the data selection radius R_{s} should correspond to the length of cracks. When the ratio R_{s}/a exceeds 0.3, then convergence in the SIF is robust.

ACKNOWLEDGMENTS

This work was supported by the NKFIH grant K143175, the TKP2021-NVA funding scheme granted by the National Research, Development, and Innovation Fund and the China Scholarship Council (202008210195).

CONFLICT OF INTEREST STATEMENT

The authors declare no potential conflict of interest.

REFERENCES

[1] Khalilpasha, H. and Albermani, F. (2013). Textured deep subsea pipelines. International Journal of Mechanical Sciences, 68, pp.224-235. DOI: 10.1016/j.ijmecsci.2013.01.019.
[2] Bolonkin, A. A. (2010). Aerial high altitude gas pipeline. Journal of Natural Gas Science and Engineering, 2(2-3), pp. 114-121. DOI: 10.1016/j.jngse.2010.04.003.
[3] Zheng, J. Y., Xu, P. and Chen, C. (1998). Investigation on bursting pressure of flat steel ribbon wound pressure vessels. International Journal of Pressure Vessels and Piping, 75(7), pp. 581-587. DOI: 10.1016/S0308-0161(98)00061-1.
[4] Chen, M., Lu, F., Wang, R., Yu, W., Wang, D., Zhang, G. and Xue, F. (2015). The probabilistic structural integrity assessment of reactor pressure vessels under pressurized thermal shock loading. Nuclear Engineering and Design, 294, pp. 93-102. DOI: 10.1016/j.nucengdes.2015.08.020.
[5] Diamantoudis, A. T. and Kermanidis, T. (2005). Design by analysis versus design by formula of high strength steel pressure vessels: a comparative study. International Journal of Pressure Vessels and Piping, 82(1), pp. 43-50. DOI: 10.1016/j.ijpvp.2004.06.0.

[6] Qasim, T., Ford, C., Bush, M. B., Hu, X., Malament, K. A. and Lawn, B. R. (2007). Margin failures in brittle dome structures: relevance to failure of dental crowns. Journal of Biomedical Materials Research Part B: Applied Biomaterials: An Official Journal of The Society for Biomaterials, The Japanese Society for Biomaterials, and The Australian Society for Biomaterials and the Korean Society for Biomaterials, 80(1), pp. 78-85. DOI: 10.1002/jbm.b.30571.

[7] Jasieńko, J., Raszczuk, K., Kleszcz, K. and Frąckiewicz, P. (2021, June). Numerical analysis of historical masonry domes: A study of St. Peter's Basilica dome, Structures, 31, pp. 80-86. Elsevier. DOI: 10.1016/j.istruc.2021.01.082.

[8] Masi, F., Stefanou, I. and Vannucci, P. (2018). On the origin of the cracks in the dome of the Pantheon in Rome. Engineering Failure Analysis, 92, pp. 587-596. DOI: 10.1016/j.engfailanal.2018.06.013.

[9] Richard, H.A., Sander, M. (2016). Damages Caused by Crack Growth. In: Fatigue Crack Growth. Solid Mechanics and Its Applications, Berlin, Springer, pp. 27–53. DOI: 10.1007/978-3-319-32534-7_2.

[10] Cao, S. and Sipos, A. A. (2022). Cracking patterns of brittle hemispherical domes: an experimental study. Frattura ed Integrità Strutturale, 59, pp. 265-310. DOI: 10.3221/IGF-ESIS.59.20.

[11] Hamed, E., Bradford, M. A., Gilbert, R. I. and Chang, Z. T. (2011). Analytical model and experimental study of failure behavior of thin-walled shallow concrete domes. Journal of Structural Engineering, 137(1), pp. 88-99. DOI: 10.1061/(ASCE)ST.1943-541X.0000274.

[12] Kurilenko, G. A. and Ayrapetyan, V. S. (2016). Determination of the fracture toughness of optomechanical devices. Optics and Photonics Journal, 6(11), pp. 298-304. DOI: 10.4236/opj.2016.611030.

[13] Farahani, B. V., Tavares, P. J., Belinha, J. and Moreira, P. M. G. P. (2017). A fracture mechanics study of a compact tension specimen: digital image correlation, finite element and meshless methods. Procedia Structural Integrity, 5, pp. 920-927. DOI: 10.1016/j.prostr.2017.07.113.

[14] Desai, C. K., Basu, S. and Parameswaran, V. (2012). Determination of complex stress intensity factor for a crack in a bimaterial interface using digital image correlation. Optics and Lasers in Engineering, 50(10), pp. 1423-1430. DOI: 10.1016/j.optlaseng.2012.05.003.

[15] Parnas, L., Bilir, Ö. G. and Tezcan, E. (1996). Strain gage methods for measurement of opening mode stress intensity factor. Engineering Fracture Mechanics, 55(3), pp. 485-492. DOI: 10.1016/0013-7944(95)00214-6.

[16] Tang, Q., Hu, J. and Yu, T. (2019). Electromagnetic evaluation of brick specimens using synthetic aperture radar imaging. NDT and E International, 104, pp. 98-107. DOI: 10.1016/j.ndteint.2019.04.006.

[17] Liu, W. and Zhang, X. (2020). An optical method for measuring mixed-mode stress intensity factors for an arbitrarily oriented crack in cylindrical shells. Theoretical and Applied Fracture Mechanics, 107, 102567. DOI: 10.1016/j.tafmec.2020.102567.

[18] Theocaris, P. S. and Thireos, C. G. (1976). Stress intensity factors in cracked cylindrical shells under tension. International Journal of Fracture, 12, pp. 691-703. DOI: 10.1007/BF00037916.

[19] Yao, X., Chen, J., Jin, G., Arakawa, K. and Takahashi, K. (2004). Caustic analysis of stress singularities in orthotropic composite materials with mode-I crack. Composites Science and Technology, 64(7-8), pp. 917-924. DOI: 10.1016/S0266-3538(02)00154-9.

[20] Theocaris, P. S. and Papadopoulos, G. A. (1980). Elastodynamic forms of caustics for running cracks under constant velocity. Engineering Fracture Mechanics, 13(4), pp. 683-698. DOI: 10.1016/0013-7944(80)90001-6.

[21] Takahashi, K. and Arakawa, K. (1987). Dependence of crack acceleration on the dynamic stress-intensity factor in polymers. Experimental Mechanics, 27, pp. 195-199. DOI: 10.1007/BF02319474.

[22] Rosakis, A. J. (1980). Analysis of the optical method of caustics for dynamic crack propagation. Engineering Fracture Mechanics, 13(2), pp. 331-347. DOI: 10.1016/0013-7944(80)90063-6

[23] Reddy, M. S., Ramesh, K. and Thiyagarajan, A. (2018). Evaluation of mode-I SIF, T-stress and J-integral using displacement data from digital image correlation–Revisited. Theoretical and Applied Fracture Mechanics, 96, pp. 146-159. DOI: 10.1016/j.tafmec.2018.04.006.

[24] Barhli, S. M., Mostafavi, M., Cinar, A. F., Hollis, D. and Marrow, T. J. (2017). J-integral calculation by finite element processing of measured full-field surface displacements. Experimental Mechanics, 57, pp. 997-1009. DOI: 10.1007/s11340-017-0275-1.

[25] Gonzáles, G. L., González, J. A., Castro, J. T. and Freire, J. L. (2017). A J-integral approach using digital image correlation for evaluating stress intensity factors in fatigue cracks with closure effects. Theoretical and Applied Fracture Mechanics, 90, pp. 14-21. DOI: 10.1016/j.tafmec.2017.02.008.

[26] Williams ML. (1957). On the stress distribution at the base of a stationary crack. Journal of Applied Mechanics,24(1), pp. 109-114. DOI: 10.1115/1.4011454.

[27] Roux, S., Réthoré, J. and Hild, F. (2009). Digital image correlation and fracture: an advanced technique for estimating stress intensity factors of 2D and 3D cracks. Journal of Physics D: Applied Physics, 42(21), 214004. DOI:10.1088/0022-3727/42/21/214004.

[28] Hamam, R., Hild, F. and Roux, S. (2007). Stress intensity factor gauging by digital image correlation: Application in cyclic fatigue. Strain, 43(3), pp. 181-192. DOI: 10.1111/j.1475-1305.2007.00345.x.
[29] Hui, C. Y. and Ruina, A. (1995). Why K? High order singularities and small scale yielding. International Journal of Fracture, 72, pp. 97-120. DOI: 10.1007/BF00042823.
[30] Roux, S. and Hild, F. (2006). Stress intensity factor measurements from digital image correlation: post-processing and integrated approaches. International Journal of Fracture, 140, pp. 141-157. DOI : 10.1007/s10704-006-6631-2.
[31] Bharadwaj, K., Sheidaei, A., Afshar, A. and Baqersad, J. (2019). Full-field strain prediction using mode shapes measured with digital image correlation. Measurement, 139, pp. 326-333. DOI: 10.1016/j.measurement.2019.03.024.
[32] Roux-Langlois, C., Gravouil, A., Baietto, M. C., Réthoré, J., Mathieu, F., Hild, F. and Roux, S. (2015). DIC identification and X-FEM simulation of fatigue crack growth based on the Williams' series. International Journal of Solids and Structures, 53, pp. 38-47. DOI: 10.1016/j.ijsolstr.2014.10.026.
[33] Réthoré, J., Roux, S. and Hild, F. (2010). Hybrid analytical and extended finite element method (HAX-FEM): A new enrichment procedure for cracked solids. International Journal for Numerical Methods in Engineering, 81(3), pp.269-285. DOI: 10.1002/nme.2691.
[34] Mokhtarishirazabad, M., Lopez-Crespo, P., Moreno, B., Lopez-Moreno, A. and Zanganeh, M. (2017). Optical and analytical investigation of overloads in biaxial fatigue cracks. International Journal of Fatigue, 100, pp. 583-590. DOI: 10.1016/j. ijfatigue.2016.12.035.
[35] Vormwald, M., Hos, Y., Freire, J. L., Gonzáles, G. L. and Díaz, J. G. (2018). Crack tip displacement fields measured by digital image correlation for evaluating variable mode-mixity during fatigue crack growth. International Journal of Fatigue, 115, pp. 53-66. DOI: 10.1016/j.ijfatigue.2018.04.030.
[36] Camacho-Reyes, A., Vasco-Olmo, J. M., James, M. N. and Diaz, F. A. (2022). Characterization of non-planar crack tip displacement fields using a differential geometry approach in combination with 3D digital image correlation. Fatigue and Fracture of Engineering Materials and Structures, 45(5), pp. 1521-1536. DOI: 10.1111/ffe.13686.
[37] Howell, P., Kozyreff, G. and Ockendon, J. (2009). Applied Solid Mechanics, 43. Cambridge University Press.
[38] Forman, R. G., Hickman, J. C. and Shivaskumar, V. (1985). Stress intensity factors for circumferential through cracks in hollow cylinders subjected to combined tension and bending loads. Engineering Fracture Mechanics, 21(3), pp. 563-571. DOI: 10.1016/S0013-7944(85)80049-7.
[39] Seitl, S., Malíková, L., Růžička, V., Moreno, B. and Lopez-Crespo, P. (2018). Williams' expansion-based approximation of the displacement field in an Al 2024 compact tension specimen reconstructed from optical measurements. Fatigue and Fracture of Engineering Materials and Structures, 41(10), pp. 2187-2196. DOI: 10.1111/ffe.12842.
[40] Seitl, S., Malíková, L., Sobek, J., Frantík, P. and Lopez-Crespo, P. (2017). Williams expansion-based approximation of the stress field in an Al 2024 body with a crack from optical measurements. Frattura ed Integrità Strutturale, 11(41), pp. 323-331. DOI: 10.3221/IGF-ESIS.41.43.
[41] Bush, A. J. (1976). Experimentally determined stress-intensity factors for single-edge-crack round bars loaded in bending: From compliance measurements, dimensionless stress-intensity factors were determined for single-edge-crack solid and hollow bars loaded in three-point bending. Experimental Mechanics, 16, pp. 249-257. DOI: 10.1007/BF02321148.
[42] Ayatollahi, M. R. and Nejati, M. (2011). An over-deterministic method for calculation of coefficients of crack tip asymptotic field from finite element analysis. Fatigue and Fracture of Engineering Materials and Structures, 34(3), pp. 159-176. DOI: 10.1111/j.1460-2695.2010.01504.x.
[43] Xiao, Q. Z. and Karihaloo, B. L. (2007). An overview of a hybrid crack element and determination of its complete displacement field. Engineering Fracture Mechanics, 74(7), pp. 1107-1117. DOI: 10.1016/j.engfracmech.2006.12.022.
[44] Kuruppu, M. D., Obara, Y., Ayatollahi, M. R., Chong, K. P. and Funatsu, T. (2014). ISRM-suggested method for determining the mode I static fracture toughness using semi-circular bend specimen. Rock Mechanics and Rock Engineering, 47, pp. 267-274. DOI: 10.1007/s00603-013-0422-7.
[45] He, Z. and Kotousov, A. (2016). On evaluation of stress intensity factor from in-plane and transverse surface displacements. Experimental Mechanics, 56, pp. 1385-1393. DOI: 10.1007/s11340-016-0176-8.
[46] Erdogan, F. and Kibler, J. J. (1969). Cylindrical and spherical shells with cracks. International Journal of Fracture Mechanics, 5(3), pp. 229-237. DOI: 10.1007/BF00184614.
[47] SHI, J. S., XU, J. Y., REN, W. B. and SU, H. Y. (2014). Research on Energy Dissipation and Fractal Characteristics of Concrete after Exposure to Elevated Temperatures under Impact Loading. Acta Armamentarii, 35(5), pp. 703-710. DOI: 10.3969/j.issn.1000-1093.2014.05.019.
[48] Levy, S. and Molinari, J. F. (2010). Dynamic fragmentation of ceramics, signature of defects and scaling of fragment sizes. Journal of the Mechanics and Physics of Solids, 58(1), pp. 12-26. DOI: 10.1016/j.jmps.2009.09.002.
[49] Zhou, F., Molinari, J. F. and Ramesh, K. T. (2006). Effects of material properties on the fragmentation of brittle materials.

International Journal of Fracture, 139(2), pp. 169-196. DOI: 10.1007/s10704-006-7135-9.
[50] Ren, W. and Xu, J. (2017). Fractal characteristics of concrete fragmentation under impact loading. Journal of Materials in Civil Engineering, 29(4), 04016244. DOI:10.1061/(ASCE)MT.1943-5533.0001764.
[51] Feng, P., Liu, B., Tang, R., Wei, M., Zhang, Y. and Li, H. (2022). Dynamic fracture behaviors and fragment characteristics of pre-compressed flawed sandstones. International Journal of Mechanical Sciences, 220, 107162. DOI: 10.1016/j.ijmecsci.2022.107162.
[52] Duggan, T. V., Byrne, J., Duggan, T. V. and Byrne, J. (1977). Fracture Mechanics and Fatigue Crack Propagation. Fatigue as a Design Criterion, pp. 112-147. DOI: 10.1007/978-1-349-03222-8_6.

NOMENCLATURE

E : Young's modulus (MPa);
α : Half-crack center angle (º);
R : Cylinder radius (mm);
G : Shear modulus (MPa);
$\varkappa$: Kolosov constant;
ν : Poisson's ratio;
(x, y, z) : Global basis;
(i, j, k) : Local basis defined by crack;
$\mathbf{U}$: x direction displacement vector (mm);
$\mathbf{V}$: y direction displacement vector (mm);
$\mathbf{W}$: z direction displacement vector (mm);
$\boldsymbol{u}$: i direction displacement vector (mm);
$\boldsymbol{v}$: j direction displacement vector (mm);
$\boldsymbol{w}$: k direction displacement vector (mm);
$\bar{u}$: i-direction displacement in the equivalent system (mm);
$\bar{v}$: j-direction displacement in the equivalent system (mm);
A_n : Coefficients of the expansion;
B_n : Coefficients of the expansion;
a : Half crack length, $a=\alpha R\pi/180^o$ (mm);
L : Cylinder length (mm);
h : Cylinder thickness (mm);
K_I : Stress intensity factor of mode I crack (MPa·mm$^{0.5}$);
K_{II} : Stress intensity factor of mode II crack (MPa·mm$^{0.5}$);
F : Dimensionless stress intensity factor;
D_N : Number of data points ;
T_N : Last term in the Williams expansion;
E_N : Excess of the number of data points over the number of terms in Williams expansion;
R_S : Data selecting ring radius (mm);
φ_c : Rigid body rotation to the crack tip